

Majorana fermions in Ge/Si hole nanowires

Franziska Maier,¹ Jelena Klinovaja,² and Daniel Loss¹

¹*Department of Physics, University of Basel, Klingelbergstrasse 82, CH-4056 Basel, Switzerland*

²*Department of Physics, Harvard University, Cambridge, Massachusetts 02138, USA*

(Dated: October 3, 2018)

We consider Ge/Si core/shell nanowires with hole states coupled to an s -wave superconductor in the presence of electric and magnetic fields. We employ a microscopic model that takes into account material-specific details of the band structure such as strong and electrically tunable Rashba-type spin-orbit interaction and g factor anisotropy for the holes. In addition, the proximity-induced superconductivity Hamiltonian is derived starting from a microscopic model. In the topological phase, the nanowires host Majorana fermions with localization lengths that depend strongly on both the magnetic and electric fields. We identify the optimal regime in terms of the directions and magnitudes of the fields in which the Majorana fermions are the most localized at the nanowire ends. In short nanowires, the Majorana fermions hybridize and form a subgap fermion whose energy is split away from zero and oscillates as a function of the applied fields. The period of these oscillations could be used to measure the dependence of the spin-orbit interaction on the applied electric field and the g factor anisotropy.

PACS numbers: 73.63.Nm; 73.21.Hb; 05.30.Pr; 71.10.Pm

I. INTRODUCTION

Quasiparticles with non-Abelian statistics are considered as auspicious candidates for topological quantum computing.¹ Among these, Majorana fermions (MFs), particles that are their own antiparticles, received a large amount of attention during the last years.^{2,3} MFs are predicted to occur in different systems such as fractional quantum Hall systems,^{1,4} topological insulators,^{5–11} nanowires with strong Rashba^{12–15} or synthetic^{16,17} spin-orbit interaction (SOI), p -wave superconductors,¹⁸ Ruderman-Kittel-Kasuya-Yosida (RKKY) systems,^{19–21} and graphenelike systems.^{22–26} Recent experiments on MFs^{27–32} were performed in Rashba nanowires (NWs) since this type of setup is relatively easy to realize. The majority of these experiments use InSb or InAs NWs because they are presumed to have strong SOI and large g factors, which are necessary prerequisites for the emergence of Majorana bound states in such wires.^{12,13} However, the direct measurement of the SOI strength in one-dimensional NWs is a challenging task³³ and has not yet been performed in the materials mentioned above. In this work we focus on a promising alternative, Ge/Si core/shell NWs carrying holes in the Ge core, in which an exceptionally strong electric-field-highly tunable Rashba SOI is expected³⁴ and in which the first signatures of a strong SOI were identified experimentally.³⁵

Ge/Si core/shell NWs, cylindrical NWs with a Ge core and Si shell, attracted a lot of attention recently.^{36–43} These NWs can be grown with high precision, i.e., with core diameters between 5 and 100 nm and shell thicknesses between 1 and 10 nm. Due to the large valence-band offset between Ge and Si, a one-dimensional (1D) hole gas forms in the core of the NW.^{37,44} The p -type symmetry of the hole Bloch states gives rise to a total angular momentum $J = 3/2$, which results in an unusually large, and electrically tunable Rashba-type SOI.³⁴

Furthermore, the holes show high mobilities,^{38,42} long mean free paths,³⁷ and Coulomb interaction strongly influences their properties.⁴⁵ Longitudinal confinement in these NWs results in tunable single and double QDs⁴⁰ with anisotropic and confinement-dependent g factors,^{46,47} in long relaxation⁴³ and coherence times⁴⁸ as well as in short SOI lengths.⁴⁹ Moreover, strongly anisotropic tunable g factors and long spin phonon relaxation times⁵⁰ were predicted as well as the usability for quantum information processing based on hole spin qubits.⁵¹ Note that strongly anisotropic and electrically tunable g factors were also observed in SiGe nanocrystals.^{52,53} Most importantly for our work, externally applied strong magnetic fields allow one to access a helical regime,³⁴ which in combination with the experimentally demonstrated proximity-induced s -wave superconductivity³⁹ makes Ge/Si core/shell NWs promising candidates to generate MFs.

In the present work, we explore the properties of MFs in Ge/Si core/shell NWs starting from a microscopic model³⁴ that captures the specific NW characteristics such as g factor anisotropy and the dependence of the induced Rashba SOI on the direction and magnitude of the electric field. We extend this microscopic model to account on the same level for a proximity-induced superconductivity, which couples hole states with opposite orbital and angular momentum. We especially focus on the tunability of the SOI that allows us to access the regimes of strong and weak SOI independently of the applied magnetic field and analyze the localization lengths of the MF wave functions in the NW regarding their dependence on magnitude and direction of the applied electric and magnetic fields. The shortest localization lengths can be expected when the fields are tuned to intermediate magnitudes. Due to the g factor anisotropy we predict the shortest localization lengths for the magnetic field pointing perpendicular to the NW axis. In a NW of finite

length, the MFs localized at two NW ends overlap⁵⁴ and hybridize into an ordinary fermion which is, generally, at nonzero energy. This energy demonstrates an oscillatory behavior^{55,56} as a function of the applied electric and magnetic fields that might be used to determine the coupling constants to the electromagnetic field. Finally, we mention in passing that while we focus here on Ge/Si core-shell nanowires, we expect our analysis also to apply (at least qualitatively) to similar structures such as Ge hat-shape nanowires grown on Si.⁵⁷

The outline of the paper is as follows. In Sec. II, we introduce the effective microscopic 1D model and derive the proximity-induced superconducting coupling of NW hole states. In Sec. III, we determine the localization lengths of MFs for a semi-infinite NW in both the strong and the weak SOI regime and identify field configurations for which the shortest localization lengths can be expected. Last, we focus on the energies of hybridized MFs in finite NWs in Sec. IV. We present our conclusions in Sec. V. Technical details are deferred to the Appendixes.

II. NANOWIRE HAMILTONIAN FOR HOLES

In this section, we describe the geometry of the system and describe the directions of the applied fields for which MFs can be expected. We introduce the microscopic model³⁴ describing holes confined to the core of Ge/Si core/shell NWs and derive an effective lowest-energy subband Hamiltonian and the associated spectrum. Next, we employ a superconductivity pairing Hamiltonian introduced for holes close to the valence-band edge in bulk material¹⁵ and derive the corresponding 1D Hamiltonian within the framework of the microscopic model and project this on the subspace of the lowest-energy subband Hamiltonian.

A. Setup

Throughout this work, we consider holes confined to the core of a Ge/Si core/shell NW with core (shell) radius R (R_s) that is positioned on top of an s -wave superconductor as sketched in Fig. 1. The NW axis is assumed to point along the z axis. We restrict ourselves to field configurations in which the electric field $\mathbf{E} = (E_x, 0, 0)$ points perpendicular to the NW axis and is parallel to the surface of the superconductor and in which the magnetic field $\mathbf{B} = (B_x, 0, B_z) \equiv B(\cos \theta, 0, \sin \theta)$ is confined to the plane spanned by \mathbf{E} and the NW axis. In this case, the SOI vector, generated by the applied electric field \mathbf{E} , points along the y axis and is always perpendicular to \mathbf{B} . As shown before,^{12,13} such a configuration is optimal for generating MFs in NWs. We note that we focus here on the case where the SOI (and the electric field \mathbf{E}) is uniform along the NW. For the effects of a nonuniform SOI we refer to Ref. [58].

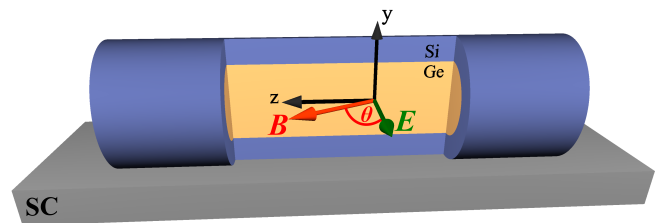


FIG. 1. Sketch of a Ge/Si core/shell NW (cylinder) placed on top of an s -wave superconductor (SC) to induce proximity pairing of the holes in the NW core. The NW axis is chosen to point along the z axis. The applied electric field $\mathbf{E} = (E_x, 0, 0)$ is parallel to the x axis, while the applied magnetic field $\mathbf{B} = (B_x, 0, B_z) \equiv B(\cos \theta, 0, \sin \theta)$ is in the xz plane.

B. Microscopic Hamiltonian

The two hole bands closest to the valence-band edge in a Ge/Si core/shell NW are described by an effective 4×4 Hamiltonian³⁴

$$H = \sum_{ij} \int dz \Psi_i^\dagger(z) (\mathcal{H}_{ij} + \mu \delta_{ij}) \Psi_j(z), \quad (1)$$

with Hamiltonian density

$$\mathcal{H} = \mathcal{H}_{\text{LK}} + \mathcal{H}_{\text{strain}} + \mathcal{H}_{\text{DR}} + \mathcal{H}_{\text{R}} + \mathcal{H}_{B,Z} + \mathcal{H}_{B,\text{orb}}, \quad (2)$$

given in the basis $\{\Psi_{g+}(z), \Psi_{g-}(z), \Psi_{e+}(z), \Psi_{e-}(z)\}$. Here, μ is a tunable chemical potential, and δ_{ij} is the Kronecker δ . The fermionic annihilation operators $\Psi_i(z) = \sum_{k_z} e^{ik_z z} c_{i,k_z}$ can be rewritten in momentum space in terms of c_{i,k_z} , which are the fermionic annihilation operators of a hole state $i \in \{g_\pm, e_\pm\}$ with momentum k_z along the NW. The index g, e refers to the ground and excited bands, and the index \pm refers to the pseudospin.

The Luttinger-Kohn and strain Hamiltonian densities are given by

$$\mathcal{H}_{\text{LK}} + \mathcal{H}_{\text{strain}} = A_+(k_z) + A_-(k_z)\tau_z + Ck_z\tau_y\sigma_x, \quad (3)$$

where τ_i and σ_i denote the Pauli matrices for band (g, e) and pseudospin index $(+, -)$, respectively. Here, $A_\pm(k_z, \eta) \equiv \hbar^2 k_z^2 (m_g^{-1} \pm m_e^{-1})/4 \pm \Delta/2$, with Planck's constant \hbar and effective masses $m_g \simeq m_0/(\gamma_1 + 2\gamma_s)$ and $m_e = m_0/(\gamma_1 + \gamma_s)$ with m_0 denoting the bare electron mass and γ_1 and γ_s representing the Luttinger parameters in spherical approximation. For Ge, $\gamma_1 = 13.35$ and $\gamma_s = 5.11$.⁵⁹ The level splitting is $\Delta \equiv \Delta_{\text{LK}} + \Delta_{\text{strain}}(\eta)$ with confinement induced $\Delta_{\text{LK}} = 0.73\hbar^2/(m_0 R^2)$ and the strain dependent splitting $\Delta_{\text{strain}}(\eta) \simeq 0 - 30$ meV, where the latter depends on the relative shell thickness $\eta \equiv (R_s - R)/R$. The off-diagonal terms, being proportional to the coupling constant $C = 7.26\hbar^2/(m_0 R)$, result directly from the strong SOI at the atomic level. The direct Rashba SOI,

$$\mathcal{H}_{\text{DR}} = eUE_x\tau_x\sigma_z, \quad U = 0.15R, \quad (4)$$

originates from the direct dipolar coupling of the hole charge to the applied electric field E_x . The conventional Rashba SOI reads

$$\mathcal{H}_R = \alpha_R E_x [S\tau_x\sigma_z + B_+(k_z) + B_-(k_z)\tau_z], \quad (5)$$

with $B_\pm(k_z) \equiv k_z T \sigma_y / 2 \pm 3k_z \sigma_y / 8$, where $T = 0.98$, $S = 0.36/R$, and $\alpha_R = -0.4 \text{ nm}^2 e$ with elementary charge e . The parameters S and U of the direct and conventional SOI, respectively, are related by $eU/(\alpha_R S) \simeq -1.1R^2 \text{ nm}^{-2}$, hence \mathcal{H}_{DR} dominates \mathcal{H}_R by one to two orders of magnitude for $R = 5 - 10 \text{ nm}$.³⁴

Finally, we include the effect of an applied magnetic field $\mathbf{B} = (B_x, 0, B_z) = B(\cos \theta, 0, \sin \theta)$ by introducing the Hamiltonian densities

$$\mathcal{H}_{B,Z} = [C_+ + C_- \tau_z] \sigma_z + [D_+ + D_- \tau_z] \sigma_x, \quad (6)$$

$$\mathcal{H}_{B,\text{orb}} = F_z \tau_x \sigma_y + F_x \tau_y. \quad (7)$$

Here, $C_\pm = \mu_B B_z (F \pm G)/2$, $D_\pm = \mu_B B_x (K \pm M)/2$, $F_z = \mu_B B_z D k_z$ and $F_x = \mu_B B_x L_B k_z$ with $F = 1.56$, $G = -0.06$, $K = 2.89$, $M = 2.56$, $D = 2.38R$, and $L_B = 8.04R$.³⁴

C. Low-energy 2×2 Hamiltonian

In this subsection, we derive an effective lowest-energy subband Hamiltonian for the holes by effectively decoupling the g_\pm and e_\pm bands introduced above in Sec. II B. To achieve this, we perform a Schrieffer-Wolff transformation^{60,61} (SWT) which block diagonalizes the Hamiltonian and subsequently allows one to truncate the lowest-energy subspace. In general, a SWT is given by a transformation of the form $H \rightarrow \tilde{H} = e^{-S} H e^S$, where S is an anti-Hermitian operator ($S^\dagger = -S$). However, we utilize the SWT in a perturbative manner and begin by subdividing the Hamiltonian density \mathcal{H} into a leading order term $\mathcal{H}_0 = A_+(0) + A_-(0)\tau_z$ and a perturbation $\mathcal{H}' = \mathcal{H} - \mathcal{H}_0$. This choice is justified since the strain induced splitting of the g_\pm and e_\pm subspaces is by far the largest energy scale present in the system. The perturbing term is further divided into a diagonal (\mathcal{H}_d) and off-diagonal part (\mathcal{H}_{od}) with respect to the two considered subspaces g_\pm and e_\pm , $\mathcal{H}' = \mathcal{H}_d + \mathcal{H}_{od}$. Next, we construct the operator S such that the SWT rotates \mathcal{H}_{od} into an approximately block-diagonal form. We also expand $e^S \approx 1 + S + S^2/2$ and then approximate S to lowest order by $S \approx S_1$, where S_1 is determined by $[S_1, \mathcal{H}_0] = \mathcal{H}_{od}$. As a result, the approximate block-diagonal Hamiltonian density $\tilde{\mathcal{H}} \approx \mathcal{H}_0 + \mathcal{H}_d - [S_1, \mathcal{H}_{od}] + [S_1, [S_1, \mathcal{H}_0]]/2$ is exact to second order in $(\mathcal{H}_{od})_{ij}/\Delta \ll 1$, where $(\mathcal{H}_{od})_{ij}$ denotes the matrix elements coupling the g_\pm and e_\pm subspaces. This corresponds to conditions restricting the magnitudes of the applied fields: $Ck_z/\Delta \ll 1$, $eUE_x/\Delta \ll 1$, $\mu_B B_x Lk_z/\Delta \ll 1$, and $\mu_B B_z Dk_z/\Delta \ll 1$. After truncating, the effective lowest-energy Hamiltonian is given by

$$\tilde{H}_{g'} = \sum_{i,j=g'_\pm} \int dz \Psi_i (\tilde{\mathcal{H}}_{g'})_{ij} \Psi_j, \text{ with density}$$

$$\tilde{\mathcal{H}}_{g'} = \begin{pmatrix} \frac{\hbar^2}{2m_{\text{eff}}} k_z^2 - \mu + \mu_B B_z g_z & \mu_B B_x g_x - iE_x k_z \alpha_{\text{eff}} \\ \mu_B B_x g_x + iE_x k_z \alpha_{\text{eff}} & \frac{\hbar^2}{2m_{\text{eff}}} k_z^2 - \mu - \mu_B B_z g_z \end{pmatrix} \quad (8)$$

in the associated low-energy basis $\{\Psi_{g'_+}, \Psi_{g'_-}\}$. The new annihilation operators are linear combinations of the original operators introduced below Eq. (2), where the associated admixing coefficients depend strongly on the NW parameters R and Δ and on the magnitude and direction of \mathbf{E} and \mathbf{B} .

In Eq. (8), we identify an effective kinetic term $\propto m_{\text{eff}}^{-1}$, an effective SOI term $\propto \alpha_{\text{eff}}$, and two terms $\propto g_x, g_z$ describing the effective coupling to the magnetic field,

$$\alpha_{\text{eff}} = T\alpha + \frac{2}{\Delta} C(eU + S\alpha), \quad \frac{\hbar^2}{2m_{\text{eff}}} \approx \frac{\hbar^2}{2m_g} - \frac{C^2}{\Delta}, \quad (9)$$

$$g_x = K - \frac{2}{\Delta} L_B C k_z^2, \quad g_z = G - \frac{2}{\Delta} D C k_z^2. \quad (10)$$

We note that m_{eff} has an additional weak dependence on \mathbf{B} which is neglected here. Furthermore, we see that the effective g factors $g_i = g_{i0} + g_{i2} k_z^2$ ($i = x, z$) differ strongly in magnitude, which leads to anisotropy, and, in addition, they depend on the momentum k_z .

The Hamiltonian $\tilde{H}_{g'}$ describes the lowest-energy subbands g'_\pm , where all coupling terms to the higher bands are taken into account by introducing effective g factors and SOI coupling. We note that the Hamiltonian density $\tilde{\mathcal{H}}_{g'}$ resembles closely the Hamiltonian densities introduced in other works^{12,13,62} to describe electrons in Rashba SOI NWs in the presence of a magnetic field. However, the dependence on the direction and strength of \mathbf{E} and \mathbf{B} is much more involved in the case of Ge/Si core/shell NWs.

The spectrum of $\tilde{H}_{g'}$ is given by

$$E_{u,d}(k_z) = \frac{\hbar^2 k_z^2}{2m_{\text{eff}}} \pm \sqrt{E_x^2 \alpha_{\text{eff}}^2 k_z^2 + \Delta_Z^2}, \quad (11)$$

where $\Delta_Z^2 = \mu_B^2 (B_x^2 g_x^2 + B_z^2 g_z^2)$ and the index u (d) marks the upper (lower) energy band. The Fermi wave vector k_F is found from the condition $E_d(k_z) = 0$ and is given by

$$k_F = \pm \sqrt{2\tilde{k}_{so}^2 + \sqrt{4\tilde{k}_{so}^4 + \tilde{k}_Z^4}}, \quad (12)$$

with components

$$\tilde{k}_{so}^2 = \frac{E_x^2 \alpha_{\text{eff}}^2 - 4(C/\Delta) [B_z^2 D G + B_x^2 K L_B] \mu_B^2}{\hbar^4 / m_{\text{eff}}^2 - 16(C/\Delta)^2 [B_z^2 D^2 + B_x^2 L_B^2] \mu_B^2}, \quad (13)$$

$$\tilde{k}_Z^4 = \frac{4 [B_z^2 G^2 + B_x^2 K^2] \mu_B^2}{\hbar^4 / m_{\text{eff}}^2 - 16(C/\Delta)^2 [B_z^2 D^2 + B_x^2 L_B^2] \mu_B^2}. \quad (14)$$

To obtain this result, we have taken into account the full k_z dependence of the g factors, hence we cannot use the

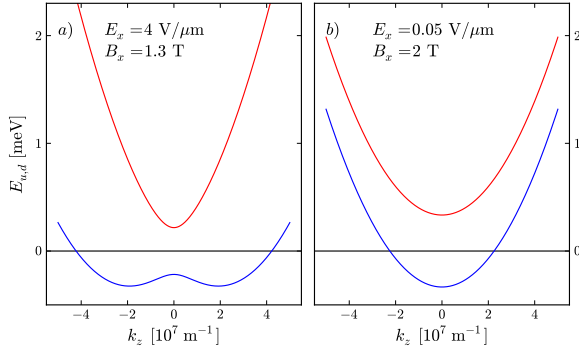


FIG. 2. The lowest-energy spectra $E_u(k_z)$ (red) and $E_d(k_z)$ (blue) as functions of the momentum k_z (a) in the strong SOI regime and (b) in the weak SOI regime. The respective magnitudes of the applied fields are given as insets. The magnetic field \mathbf{B} is chosen along the x axis (like the \mathbf{E} field). The used NW parameters are $R = 7.5$ nm and $\Delta = 23$ meV.

effective parameters g_x and g_z as they themselves depend on k_z [see Eq. (10)]. Using the definitions above, we introduce the SOI energy $\tilde{\Delta}_{so} = E_x \alpha_{\text{eff}} \tilde{k}_{so}/2$. This allows us to distinguish between the strong SOI regime ($k_F/\tilde{k}_{so} \approx 2$), where the SOI energy dominates over the Zeeman energy, and the weak SOI regime ($k_F/\tilde{k}_Z \approx 1$), where the Zeeman energy dominates over the SOI energy. In Fig. 2, we plot the bands $E_{u,d}(k_z)$ for two sets of finite electric and magnetic fields: one in the strong [Fig. 2(a)] and one in the weak [Fig. 2(b)] SOI regime. We compared numerically the exact spectrum with the approximate one for the configurations considered in Fig. 2 and found good agreement.

D. Superconductivity: Pairing Hamiltonian

In this section, we derive an effective Hamiltonian describing the proximity induced superconductivity in the lowest subband g' . The proximity-induced superconducting pairing gap $\Delta_{sc}^{\text{exp}} \approx 235$ μeV was observed experimentally in Ge/Si core/shell NWs.³⁸ Pairing Hamiltonians describing superconductivity for hole states in semiconductors were also discussed before in several theoretical works.^{15,63,64} Here, we start from a general pairing Hamiltonian allowing for coupling between bulk hole states with opposite orbital and angular momentum,¹⁵

$$H_{SC} = \int d^3r \left[\Delta_{3/2} \Psi_{3/2}^\dagger \Psi_{-3/2}^\dagger + \Delta_{1/2} \Psi_{1/2}^\dagger \Psi_{-1/2}^\dagger + \text{H.c.} \right], \quad (15)$$

where the fermionic operators Ψ_{m_j} annihilate bulk hole states with angular momentum $j = 3/2$ and $m_j = \pm 3/2, \pm 1/2$ and which are coupled by the respective superconducting pairing potentials $\Delta_{3/2}$ and $\Delta_{1/2}$. We assume that $\Delta_{3/2}$ is real but employ $\Delta_{1/2} = |\Delta_{1/2}|e^{i\varphi_{sc}}$ to

account for a possible complex superconducting phase. We use H_{SC} to derive an effective pairing Hamiltonian within the framework of the microscopic model (see Sec. IIB) by modifying the procedure outlined in Ref. [34]. By extending the basis of the microscopic model given below Eq. (2) accordingly, we derive an effective 1D particle-hole basis.⁶⁵ Furthermore, we use the explicit three-dimensional wave functions of the hole states in the NW³⁴ and calculate the matrix elements of the effective 1D superconducting Hamiltonian by integrating out the transverse part. Finally, we transform the resulting Hamiltonian by the SWT introduced in Sec. IIC and truncate the lowest-energy particle-hole subspace with Nambu space representation $\Psi_{ph} = (\Psi_{g'_+}, \Psi_{g'_-}, \Psi_{g'_+}^\dagger, \Psi_{g'_-}^\dagger)$. In this representation, the effective lowest-energy subband superconducting pairing Hamiltonian is given by $\tilde{H}_{SC} = \frac{1}{2} \int dz \Psi_{ph}^\dagger \tilde{\mathcal{H}}_{SC} \Psi_{ph}$ with

$$\tilde{\mathcal{H}}_{SC} = \begin{pmatrix} 0 & 0 & 0 & i\Delta_{sc} \\ 0 & 0 & -i\Delta_{sc} & 0 \\ 0 & i\Delta_{sc}^* & 0 & 0 \\ -i\Delta_{sc}^* & 0 & 0 & 0 \end{pmatrix}, \quad (16)$$

where $i\Delta_{sc} = 0.01\Delta_{3/2} - 0.5|\Delta_{1/2}|e^{i\varphi_{sc}}$. We combine $\tilde{\mathcal{H}}_{SC}$ with $\tilde{\mathcal{H}}_{g'}$, where the latter is extended to the particle-hole subspace Ψ_{ph} , and obtain an effective Bogoliubov-de Gennes Hamiltonian (explicitly given in Appendix A). The spectrum of this Hamiltonian is given by

$$E^2 = \left(\frac{\hbar^2 k_z^2}{2m_{\text{eff}}} \right)^2 + E_x^2 k_z^2 \alpha_{\text{eff}}^2 + \Delta_Z^2 + |\Delta_{sc}|^2 + 2\sqrt{\left(\frac{\hbar^2 k_z^2}{2m_{\text{eff}}} \right)^2 (E_x^2 k_z^2 \alpha_{\text{eff}}^2 + \Delta_Z^2) + |\Delta_{sc}|^2 \Delta_Z^2}. \quad (17)$$

At $k_z = 0$, we find that Eq. (17) reduces to $E^2 = (|\Delta_{sc}| \pm \Delta_Z)^2$, and the topological gap is given by

$$\Delta_- = |\Delta_{sc}| - \Delta_Z. \quad (18)$$

The system is in the nontopological phase for $\Delta_- > 0$ and in the topological phase for $\Delta_- < 0$.^{12,13,62}

III. TUNABILITY OF THE MF LOCALIZATION LENGTH

Next, we focus on the MF wave functions and associated localization lengths assuming that the two MFs are well localized at the ends of a Ge/Si core/shell NW and do not overlap with each other. To obtain independent solutions for the MF wave functions at both ends, we simplify the calculations by assuming a semi-infinite NW originating, let's say, at $z = 0$. For topological computational schemes, one generally strives for small localization lengths and, thus, well localized MFs. We analyze the tunability of the localization lengths as functions of magnitude and direction of the applied fields \mathbf{E} and \mathbf{B} and

determine the regime in which the localization lengths are the shortest.

A. Strong SOI

First, we focus on the strong SOI regime, where $\Delta_{so} \gg \Delta_Z$ with $\Delta_{so} = \alpha_{\text{eff}} E_x k_{so}/2$ and $k_{so} = m_{\text{eff}} \alpha_{\text{eff}} E_x / \hbar^2$. Here, the Fermi wave number is given by $k_F^s = 2k_{so}$, and the associated Fermi velocity is $v_F^s = \alpha_{\text{eff}} E_x / \hbar$. In this regime, the main effect of the applied magnetic field is the opening of a gap at $k_z = 0$, thus we are allowed to drop the k_z dependence of the g factors [see Eqs. (10)] and to use the following approximation for the Zeeman splitting $\Delta_Z \approx \Delta_Z^0 e^{i\vartheta_B^0} = \mu_B (B_x g_{x0} + i B_z g_{z0})$. To derive the MF wave functions,⁶² we first linearize the spectrum around the Fermi points $k_z = 0$ (interior branch of the spectrum) and $k_z = \pm k_F^s$ (exterior branch of the spectrum) and express the fermionic operators in terms of slowly varying left and right movers L_{\pm} and R_{\pm} where the indices \pm label the two pseudospin directions for a quantization axis pointing along the SOI induced by the electric field E_x . As a result, the Hamiltonian splits into two independent parts. The exterior branch is described by

$$\mathcal{H}^e = i\hbar v_F^s \eta_0 \nu_z \partial_z + \frac{1}{2} [i\Delta_{sc}(\eta_x + i\eta_y)\nu_y + \text{H.c.}], \quad (19)$$

which is written in the basis $(L_+, R_-, L_+^\dagger, R_-^\dagger)$. Here, the Pauli matrices η_i (ν_i), $i = 0, x, y, z$, act in particle-hole (left and right mover) subspace. The interior branch is described by

$$\begin{aligned} \mathcal{H}^i = & -i\hbar v_F^s \eta_0 \nu_z \partial_z + \frac{1}{2} [i\Delta_{sc}(\eta_x + i\eta_y)\nu_y + \text{H.c.}] \\ & - \Delta_Z^0 (\cos \vartheta_B^0 \eta_0 \nu_y + \sin \vartheta_B^0 \eta_z \nu_x), \end{aligned} \quad (20)$$

which is given in the basis $(R_+, L_-, R_+^\dagger, L_-^\dagger)$. As shown before, a localized zero energy state, MF, exists in the topological phase $\Delta_Z^0 > |\Delta_{sc}|$. The associated MF wave function is a sum of two contributions,⁶² $\hat{\Phi}_s(z) = \hat{\Phi}_s^e(z) + \hat{\Phi}_s^i(z)$, originating from the exterior and interior branches (for an explicit expression see Appendix B 1), which are of the form

$$\hat{\Phi}_s^e(z) \propto e^{-z/\xi_s^e}, \quad \hat{\Phi}_s^i(z) \propto e^{-z/\xi_s^i}, \quad (21)$$

with the localization lengths given by

$$\xi_s^e = \frac{\alpha_{\text{eff}} |E_x|}{|\Delta_{sc}|}, \quad \xi_s^i = \frac{\alpha_{\text{eff}} |E_x|}{|\Delta_-|}. \quad (22)$$

Both ξ_s^e and ξ_s^i depend linearly on the magnitude of the applied electric field E_x , thus weaker fields result in smaller localization lengths. Furthermore, ξ_s^i shows an implicit dependence on the magnitude and direction of \mathbf{B} in the denominator via $\Delta_- = |\Delta_{sc}| - \Delta_Z^0$. The localization length diverges when Δ_Z^0 approaches $|\Delta_{sc}|$, which

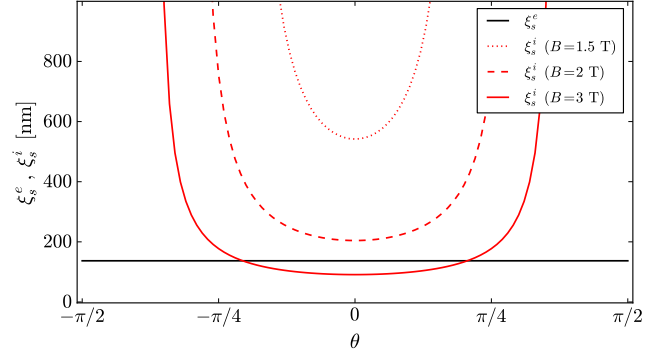


FIG. 3. Localization lengths ξ_s^e and ξ_s^i as functions of the angle θ defined by $\mathbf{B} = B(\cos \theta, 0, \sin \theta)$, for $E_x = 4 \text{ V}/\mu\text{m}$ and for different magnitudes of B . As soon as θ deviates from 0, ξ_s^i increases until it diverges when the topological gap closes. Furthermore, increasing B above a threshold value given by $|\Delta_-| = |\Delta_{sc}|$, i.e. $\Delta_Z^0 \geq 2|\Delta_{sc}|$, results in $\xi_s^i < \xi_s^e$ for a certain range of θ . Since ξ_s^e is independent of \mathbf{B} , its value appears as a constant in the plot. We use the NW parameters $R = 7.5 \text{ nm}$ and $\Delta = 23 \text{ meV}$ and assume a superconductivity pairing potential of $\Delta_{sc} = 200 \mu\text{eV}$.

happens when the topological gap closes and the system becomes gapless. In Fig. 3, we plot ξ_s^e and ξ_s^i as functions of the angle θ enclosed by \mathbf{B} and the x axis (see Fig. 1). We see that as soon as \mathbf{B} has a nonzero component parallel to the NW, ξ_s^i increases until it diverges at the point where the topological gap closes and the system goes into the topologically trivial phase. This effect roots in the strong anisotropy of the g factor in Δ_Z^0 which leads to a quick closing of the topological gap as soon as θ deviates from zero. Furthermore, increasing the magnitude of \mathbf{B} while still being in the strong SOI regime, such that $|\Delta_-| > |\Delta_{sc}|$, i.e. $\Delta_Z^0 \geq 2|\Delta_{sc}|$, results in $\xi_s^i < \xi_s^e$ for a certain range of θ . Thus, in this regime, the localization length of the MF wave functions, $\xi = \max\{\xi_s^i, \xi_s^e\}$, is independent of the magnetic field.

B. Weak SOI

Next, we focus on the weak SOI regime in which $\Delta_{so} \ll \Delta_Z$. We find that $\Delta_Z \sim \Delta_Z^0$ is still a good approximation for magnetic fields up to $B \sim 5 \text{ T}$. This allows us to simplify Eq. (12). As a result, the Fermi wave number is given by $k_F^w \approx \sqrt{2m_{\text{eff}}\Delta_Z^0}/\hbar$, and the associated Fermi velocity reads $v_F^w = \sqrt{2\Delta_Z^0/m_{\text{eff}}}$. By treating the SOI as a weak perturbation, we find the eigenstates of the particle Hamiltonian around the Fermi points k_F^w and linearize the particle-hole Hamiltonian in the basis constructed of these states. We find

$$\mathcal{H}^{(e)} = -i\hbar v_F^w \eta_0 \nu_z \partial_z + \frac{1}{2} [\bar{\Delta}_{sc}^* e^{-i\vartheta_B^0} (\eta_x + i\eta_y) \nu_y + \text{H.c.}], \quad (23)$$

which is represented in the basis $(R, L, R^\dagger, L^\dagger)$, with $R(L)$ being the right mover (left mover) in the weak

SOI regime. As already found in Ref. [62], the effective coupling due to superconductivity is suppressed by a factor $k_{so}/k_F^w \ll 1$, resulting in an effective superconducting coupling term $|\bar{\Delta}_{sc}| = 2|\Delta_{sc}|k_{so}/k_F^w$. This can be understood from the fact that without the SOI, the pseudospins of the states at the Fermi points are perfectly aligned and only the weakly perturbing SOI term tilts them into a slightly nonparallel configuration that enables a superconducting pairing. The localized MF wave function is again a sum of two contributions, $\hat{\Phi}_w(z) = \hat{\Phi}_w^{(e)}(z) + \hat{\Phi}_w^{(i)}(z)$ (for an explicit expression see Appendix B 2), which are of the form

$$\hat{\Phi}_w^{(e)}(z) \propto e^{-z/\xi_w^{(e)}}, \quad \hat{\Phi}_w^{(i)}(z) \propto e^{-z/\xi_w^{(i)}}, \quad (24)$$

with localization lengths given by

$$\xi_w^{(e)} = \sqrt{\frac{2\Delta_Z^0}{m_{\text{eff}}|\bar{\Delta}_{sc}|}} \frac{\hbar}{|\Delta_{sc}|} = \frac{\Delta_Z^0}{|\Delta_{sc}|} \frac{\hbar^2}{m_{\text{eff}}\alpha_{\text{eff}}|E_x|},$$

$$\xi_w^{(i)} = \frac{\alpha_{\text{eff}}|E_x|}{|\Delta_{sc}|}. \quad (25)$$

We see that the localization lengths depend quite differently on the strength of the SOI determined by E_x , $\xi_w^{(e)} \propto 1/|E_x|$ and $\xi_w^{(i)} \propto |E_x|$. Furthermore, in contrast to the strong SOI regime, both localization lengths depend on the magnitude and direction of \mathbf{B} . In Fig. 4, we plot $\xi_w^{(e)}$ and $\xi_w^{(i)}$ as functions of the angle θ enclosed by \mathbf{B} and the x axis, for various combinations of E_x and B . We observe that the dependence of $\xi_w^{(e)}$ on θ is much weaker than the θ dependence of $\xi_w^{(i)}$, e.g., $\xi_w^{(e)}$ does not diverge when the topological gap closes. Furthermore, depending on the relative magnitude of the fields, we can find both, $\xi_w^{(e)} > \xi_w^{(i)}$ and $\xi_w^{(e)} < \xi_w^{(i)}$.

C. Optimal experimental regime

As shown above, the magnitude and direction of the applied fields determine the localization lengths of the MF wave functions; see Figs. 3 and 4. In experiments, it is crucial to tune the applied fields such that obtained MFs are well separated and the localization lengths are as short as possible. To identify the optimal field regime, we display the logarithm of the maximal localization length for the given magnitudes of the applied fields in Fig. 5. In the weak SOI regime, we furthermore have to take into account that the part of the wave function decaying with the localization length $\xi_s^{(i)}$ is additionally suppressed by a factor $k_{so}/k_F^w \ll 1$ and thus can be neglected. To simplify the analysis, we fix the direction of the magnetic field to be perpendicular to the NW, $\mathbf{B} = (B_x, 0, 0)$. Here, we are motivated by the fact that this configuration corresponds to the shortest localization lengths in the strong SOI regime. The range of B_x is chosen such that we remain in the topological regime throughout. We see that when applying large E_x while keeping B_x small

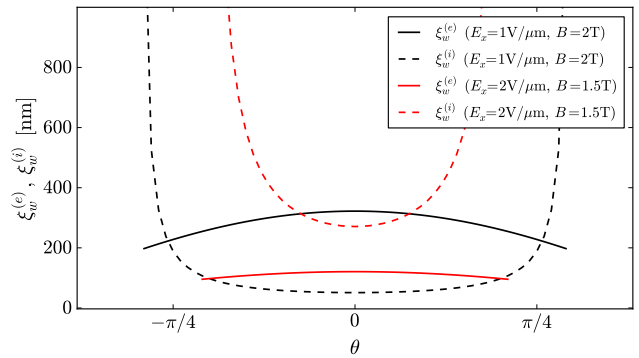


FIG. 4. Localization lengths $\xi_w^{(e)}$ and $\xi_w^{(i)}$ as functions of the angle θ defined by $\mathbf{B} = B(\cos \theta, 0, \sin \theta)$, for different magnitudes of E_x and B . Here we use the combinations $E_x = 1 \text{ V}/\mu\text{m}$ and $B = 2 \text{ T}$ (black), $E_x = 2 \text{ V}/\mu\text{m}$ and $B = 1.5 \text{ T}$ (red). As soon as θ deviates from 0, $\xi_w^{(i)}$ increases until its value diverges when the topological gap closes. In contrast to ξ_s^e (see Fig. 3), $\xi_w^{(e)}$ now shows a dependence on θ . Here, we use the same values for the NW parameters and superconducting pairing parameter as in Fig. 3.

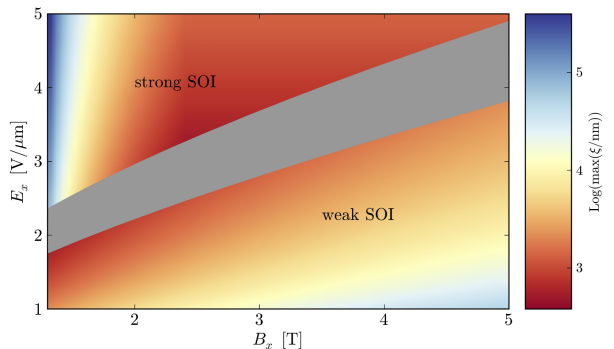


FIG. 5. Logarithm (color coded) of the dominating localization length, $\xi = \max\{\xi_s^e, \xi_s^i\}$ and ξ_w^e , in the strong and weak SOI regime, respectively, as functions of the applied fields E_x and B_x . For simplicity we restrict ourselves to $\mathbf{B} = (B_x, 0, 0)$. The diagonal gray area approximately denotes the transitional regime between regions of strong and weak SOI. Here, we use the same values for the NW parameters and superconducting pairing parameter as in Fig. 3.

or when applying large B_x while keeping E_x small, the localization lengths are not the shortest possible. Hence it is most favorable to choose an intermediate regime in which both fields take rather moderate values and the Zeeman energy and the SOI energy are comparable with each other.

IV. FINITE NANOWIRES: HYBRIDIZED MAJORANA FERMIONS

So far we have focused on a semi-infinite NW that, when being brought into the topological phase, hosts a

zero-energy MF at the end. However, in any realistic system, the NWs are of finite length L and host two MFs: one MF at each end. These MFs could overlap and hybridize if their localization lengths are comparable with the NW length. This results in the emergence of an ordinary fermion which, in general, possesses a nonzero energy.^{55,56} In this section, we examine the dependence of this fermionic energy on the magnitude of the applied fields in the strong and weak SOI regime. We assume that the NW stretches from $z = 0$ to $z = L$ and search for hybridized wave functions that satisfy vanishing boundary conditions at both ends of the NW. We note that we focus here on the direct overlap between two MF wave functions and neglect a possible hybridization mediated by bulk superconducting states.⁶⁶

A. Strong SOI

In this section, we explore the energy of hybridized MFs in the strong SOI regime. First, we solve the Schrödinger equations $\mathcal{H}^e \phi^e = E_n^s \phi^e$ and $\mathcal{H}^i \phi^i = E_n^s \phi^i$ for arbitrary $E_n^s > 0$ (for the Hamiltonian densities see Sec. III A). Since the NW is of finite length, both the decaying and growing eigenfunctions are normalizable and may contribute to the final hybridized wave function. We obtain a set of eight eigenfunctions ϕ_j^e and ϕ_j^i , $j = 1, \dots, 4$, where the ϕ_j^e show an oscillatory behavior proportional to $e^{\pm i k_F z}$. We search for a nontrivial linear combination of these eigenfunctions, $\Phi_{\text{hyb}}^s(z) = \sum_j (a_j^e \phi_j^e + a_j^i \phi_j^i)$, that satisfies the boundary conditions $\Phi_{\text{hyb}}^s(z=0) = \Phi_{\text{hyb}}^s(z=L) = 0$. In the considered regime, E_n^s is given by a quite involved implicit equation which we omit displaying here.

We provide numerical results for several specific sets of applied fields and plot E_n^s as a function of E_x in Fig. 6. For all field configurations, we observe an oscillatory behavior of E_n^s with increasing amplitude as E_x increases. In addition, depending on the magnitude of the applied magnetic field, the curves may show a nonzero offset that increases with E_x . This feature is the most pronounced for small magnetic fields close to the point where the topological gap closes.

These results can be explained easily when remembering the zero energy MF wave function which is a linear combination of oscillating (exterior branch, ξ_s^e) and nonoscillating (interior branch, ξ_s^i) wave functions (see Sec. III A). This result remains valid for very small energies E_n^s , thus the lengthscales governing the growth and decay of the eigenstates $\phi_j^{e,i}$ are comparable to ξ_s^e and ξ_s^i . If the localization length is set by the nonoscillating interior branch part, $\xi_s^e/\xi_s^i \ll 1$ (the respective ratios are included in each plot in Fig. 6), E_n^s monotonically splits away from zero with superimposed weak oscillations. On the contrary, if the localization length is set by the strongly oscillating exterior branch part, $\xi_s^e/\xi_s^i \geq 1$, E_n^s oscillates strongly and even goes back to zero. Thus,

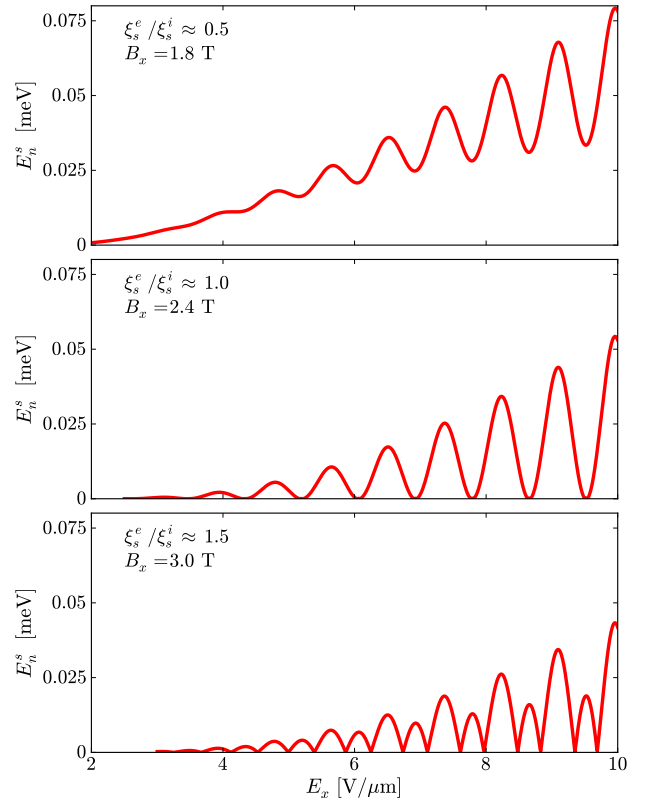


FIG. 6. The fermion energy E_n^s in the strong SOI regime as a function of the electric field E_x for different magnitudes of the applied magnetic field $\mathbf{B} = (B_x, 0, 0)$; see the insets. We consider three different ratios of the localization lengths ξ_s^e/ξ_s^i . If the contribution of the interior branches is dominant, $\xi_s^i > \xi_s^e$, E_n^s shows an increasing offset from zero with weak superimposed oscillations on top of it. If the contribution of the exterior branches is dominant, $\xi_s^e > \xi_s^i$, E_n^s shows an increasing offset from zero with strong superimposed oscillations on top of it such that E_n^s periodically returns to zero. Here, we assume a superconducting pairing potential $\Delta_{sc} = 200 \mu\text{eV}$ and use the NW parameters $R = 7.5 \text{ nm}$, $\Delta = 23 \text{ meV}$, and $L = 0.7 \mu\text{m}$.

depending on the ratio of the localization lengths ξ_s^e and ξ_s^i which can be tuned by changing the magnitude or the direction of the applied magnetic field with respect to the NW (see Fig. 3), the offset of E_n^s can be tuned. The period of the superimposed oscillations is independent of the magnitude of B_x since the ϕ_j^e cause oscillations with a period $\delta E_x = \hbar^2 \pi / (m_{\text{eff}} \alpha_{\text{eff}} L)$. Using the latter relation, the strength of the SOI can be determined from the oscillation period.

B. Weak SOI

In the weak SOI regime, we apply the same procedure as described in Sec. IV A. Here, we employ the Hamil-

tonian $\mathcal{H}^{(e)}$ given in Eq. (23) and solve the Schrödinger equation $\mathcal{H}^{(e)}\phi^{(e)} = E_n^w\phi^{(e)}$ for an arbitrary $E_n^w > 0$. The four eigenstates $\phi_j^{(e)}$, $j = 1, \dots, 4$, are combined into a nontrivial linear combination, $\Phi_{\text{hyb}}^w(z) = \sum_j b_j^{(e)}\phi_j^{(e)}$, that satisfies the boundary conditions $\Phi_{\text{hyb}}^w(z=0) = \Phi_{\text{hyb}}^w(z=L) = 0$. This leads to an implicit condition for E_n^w ,

$$\left[\frac{\sqrt{\Delta_{sc}^2 - E_n^2}}{\Delta_{sc}} \right]^2 = \frac{2 \sinh^2 \left[\frac{L\sqrt{\Delta_{sc}^2 - E_n^2}}{v_F^w \hbar} \right]}{\cosh \left[\frac{2L\sqrt{\Delta_{sc}^2 - E_n^2}}{v_F^w \hbar} \right] - \cos(2k_F^w L)}. \quad (26)$$

This implicit equation can be transformed to an explicit relation for E_n^w by assuming that $E_n^w \ll \bar{\Delta}_{sc}$,

$$E_n^w \approx \bar{\Delta}_{sc} |\sin(k_F^w L)| e^{-L/\xi_w^{(e)}}, \quad (27)$$

which shows an oscillatory behavior of E_n^w as a function of k_F^w , where the latter is a function of \mathbf{B} . In Fig. 7, we plot E_n^w as a function of $\mathbf{B} = (B_x, 0, 0)$ for a weak electric field E_x where we obtained E_n^w once by solving Eq. (26) numerically and once by using the explicit relation given in Eq. (27). Both results agree well, especially for small B_x . We see that E_n^w oscillates and the energy of the fermion composed of two overlapping MFs periodically comes back to zero.^{55,56} The periodicity of the oscillation is given by

$$\delta\Delta_Z^0 \approx \frac{\pi\hbar}{L} \sqrt{\frac{2\Delta_Z^0}{m_{\text{eff}}}}, \quad (28)$$

and depends on the g factor and hence on the direction of the magnetic field. As a result, the change in the period as a function of the magnetic field direction could be used to measure the g factor anisotropy.

Changing the strength of the applied electric field E_x does not affect the period of the oscillation, however, examining Eq. (27) in more detail shows that a stronger field E_x yields a smaller amplitude of the splitting.

V. CONCLUSION

In this work, we utilized a concrete microscopic model to study MFs confined to Ge/Si core/shell NWs. To this end, we derived an effective 1D lowest subband hole Hamiltonian, which also includes the superconducting pairing and takes into account specifics of Ge/Si core/shell NWs such as the g factor anisotropy and the electric field dependence of the induced Rashba SOI. We have determined the MF localization lengths in the strong and in the weak SOI regime and examined their dependence on the direction of the magnetic field with

respect to the NW. In general, we found that intermediate magnitudes of electric and magnetic fields lead to the shortest localization lengths of the MF wave functions. Additionally, we examined finite NWs, where two

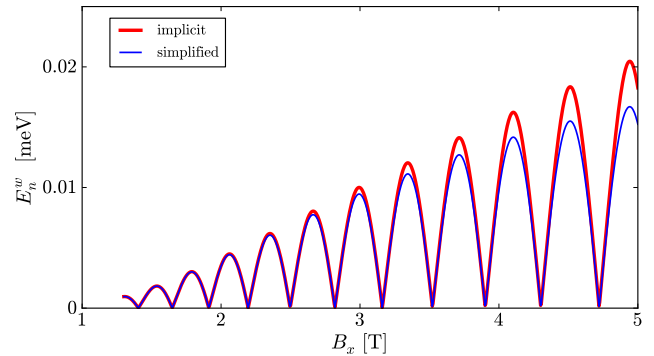


FIG. 7. The oscillating energy E_n^w as a function of $\mathbf{B} = (B_x, 0, 0)$. We display both the results from solving the implicit Eq. (26) numerically (red) and the simplified solution given in Eq. (27) (blue) and find good agreement. We assume a weak electric field $E_x = 0.5$ V/ μm and a proximity induced superconducting pairing potential $\Delta_{sc} = 200$ μeV . We use the NW parameters $R = 7.5$ nm, $\Delta = 23$ meV, and $L = 2$ μm .

MFs localized at the NW ends overlap and form an ordinary fermion. This hybridization results in a fermion whose energy oscillates as a function of the electric field (magnetic field) in the strong (weak) SOI regime. The possibility to control the overlap of MFs by tuning only electric fields could be used to perform topologically non-protected operations on Majorana fermion that are necessary to realize universal quantum computation.²

From our results we conclude that Ge/Si core/shell NWs are a promising system regarding the emergence of MFs due to the high control over the SOI strength. In addition, we note that these NWs are also excellent candidates for parafermion setups which require even stronger SOI and substantial electron-electron interactions.^{67–69} In addition, the lowest energy subband Hamiltonian derived in this work can provide the basis for further investigation of arrays of Ge/Si NWs. Such arrays could also be used to study quantum Hall effect,^{70–74} topological superconductor,^{75,76} and quantum spin Hall effect⁷⁷ in the anisotropic limit.

ACKNOWLEDGMENTS

We thank Christoph Kloeffer for helpful discussions. We acknowledge support from the Swiss NSF, NCCR QSIT, through the EC FP7-ICT initiative under project SiSPIN No. 323841, and the Harvard Quantum Optical Center.

Appendix A: Particle-hole coupling Hamiltonian

In this section, we display the effective Bogoliubov-de Gennes Hamiltonian for holes in the lowest-energy subband. To allow for a direct comparison with previous results,⁶² we rotate the lowest-energy basis Ψ_{ph} [introduced above Eq. (16)] such that the spin quantization axis lies parallel to the applied electric field E_x and the new particle-hole basis reads $\tilde{\Psi}_{ph} = (\Psi_+, \Psi_-, \Psi_+^\dagger, \Psi_-^\dagger)$, where the \pm denotes the pseudospin of the SOI split subband. The Hamiltonian is given by $\tilde{H}_{ph} = \frac{1}{2} \int \tilde{\Psi}_{ph}^\dagger \tilde{\mathcal{H}}_{ph} \tilde{\Psi}_{ph}$ with Hamiltonian density

$$\tilde{\mathcal{H}}_{ph} = \begin{pmatrix} \frac{\hbar^2 k_z^2}{2m_{\text{eff}}} - \mu + E_x \alpha_{\text{eff}} k_z & i\Delta_Z e^{i\vartheta_B} & 0 & \Delta_{sc} \\ -i\Delta_Z e^{-i\vartheta_B} & \frac{\hbar^2 k_z^2}{2m_{\text{eff}}} - \mu - E_x \alpha_{\text{eff}} k_z & -\Delta_{sc} & 0 \\ 0 & -\Delta_{sc}^* & -\frac{\hbar^2 k_z^2}{2m_{\text{eff}}} + \mu + E_x \alpha_{\text{eff}} k_z & i\Delta_Z e^{-i\vartheta_B} \\ \Delta_{sc}^* & 0 & -i\Delta_Z e^{i\vartheta_B} & -\frac{\hbar^2 k_z^2}{2m_{\text{eff}}} + \mu - E_x \alpha_{\text{eff}} k_z \end{pmatrix}. \quad (\text{A1})$$

Here, we used the abbreviation $\Delta_Z e^{i\vartheta_B} = \mu_B (B_x g_x + i B_z g_z)$. A similar Hamiltonian was used in Ref. [62] to derive MF wave functions in NWs with proximity-induced superconductivity. Note that our model additionally includes a complex superconducting pairing potential and a Zeeman term reflecting the anisotropy of the g factor of the NW.

Appendix B: Wave functions

Here we display the explicit form of the MF wave functions in both the strong and weak SOI regime.

1. Strong SOI

In the strong SOI regime, the MF wave function introduced above Eq. (21) in Sec. III A is given by

$$\hat{\Phi}_s(z) = e^{-i\pi/4} e^{-z/\xi_s^e} \begin{pmatrix} i e^{i\vartheta_B^0/2} e^{ik_F^s z} \\ -i e^{-i\vartheta_B^0/2} e^{-ik_F^s z} \\ e^{-i\vartheta_B^0/2} e^{-ik_F^s z} \\ -e^{i\vartheta_B^0/2} e^{ik_F^s z} \end{pmatrix} + e^{-i\pi/4} e^{-z/\xi_s^i} \begin{pmatrix} -i e^{i\vartheta_B^0/2} \\ i e^{-i\vartheta_B^0/2} \\ -e^{-i\vartheta_B^0/2} \\ e^{i\vartheta_B^0/2} \end{pmatrix}, \quad (\text{B1})$$

where $\hat{\Phi}_s(z)$ is written in the basis $\tilde{\Psi}_{ph}$ (see Appendix A).

2. Weak SOI

In the weak SOI regime, the MF wave function introduced above Eq. (24) in Sec. III B is given by

$$\begin{aligned} \hat{\Phi}_w(z) = \frac{1}{\sqrt{2}} e^{-z/\xi_w^{(e)}} & \begin{pmatrix} e^{i\vartheta_B^0/2} \left[\left(1 - \frac{k_{so}}{k_F^w}\right) \left(1 - i \frac{k_{so}}{k_F^w}\right) e^{ik_F^w z} - \left(1 + \frac{k_{so}}{k_F^w}\right) \left(1 + i \frac{k_{so}}{k_F^w}\right) e^{-ik_F^w z} \right] \\ e^{-i\vartheta_B^0/2} \left[\left(1 + \frac{k_{so}}{k_F^w}\right) \left(i + \frac{k_{so}}{k_F^w}\right) e^{ik_F^w z} - \left(1 - \frac{k_{so}}{k_F^w}\right) \left(i - \frac{k_{so}}{k_F^w}\right) e^{-ik_F^w z} \right] \\ e^{-i\vartheta_B^0/2} \left[\left(1 - \frac{k_{so}}{k_F^w}\right) \left(1 + i \frac{k_{so}}{k_F^w}\right) e^{-ik_F^w z} - \left(1 + \frac{k_{so}}{k_F^w}\right) \left(1 - i \frac{k_{so}}{k_F^w}\right) e^{ik_F^w z} \right] \\ e^{i\vartheta_B^0/2} \left[\left(1 + \frac{k_{so}}{k_F^w}\right) \left(-i + \frac{k_{so}}{k_F^w}\right) e^{-ik_F^w z} - \left(1 - \frac{k_{so}}{k_F^w}\right) \left(-i - \frac{k_{so}}{k_F^w}\right) e^{ik_F^w z} \right] \end{pmatrix} \\ + 2e^{-z/\xi_w^{(i)}} \frac{k_{so}}{k_F^w} e^{-i\pi/4} & \begin{pmatrix} -i e^{i\vartheta_B^0/2} \\ i e^{-i\vartheta_B^0/2} \\ -e^{-i\vartheta_B^0/2} \\ e^{i\vartheta_B^0/2} \end{pmatrix}, \end{aligned} \quad (\text{B2})$$

where $\hat{\Phi}_w(z)$ is written in the basis $\tilde{\Psi}_{ph}$ (see Appendix A). For very weak SOI ($k_{so}/k_F^w \ll 1$) the MF wave function simplifies to

$$\hat{\Phi}_w(z) \approx \sqrt{2} \sin(k_F^w z) e^{-z/\xi_w^{(e)}} \begin{pmatrix} ie^{i\vartheta_B^0/2} \\ -e^{-i\vartheta_B^0/2} \\ -ie^{-i\vartheta_B^0/2} \\ -e^{i\vartheta_B^0/2} \end{pmatrix}. \quad (\text{B3})$$

-
- ¹ C. Nayak, S. H. Simon, A. Stern, M. Freedman, and S. Das Sarma, *Rev. Mod. Phys.* **80**, 1083 (2008).
² J. Alicea, *Rep. Prog. Phys.* **75**, 076501 (2012).
³ C. Beenakker, *Annu. Rev. Condens. Matter Phys.* **4**, 113 (2013).
⁴ N. Read and D. Green, *Phys. Rev. B* **61**, 10267 (2000).
⁵ L. Fu and C. L. Kane, *Phys. Rev. Lett.* **100**, 096407 (2008).
⁶ M. Sato and S. Fujimoto, *Phys. Rev. B* **79**, 094504 (2009).
⁷ Y. Tanaka, T. Yokoyama, and N. Nagaosa, *Phys. Rev. Lett.* **103**, 107002 (2009).
⁸ S. Sasaki, M. Kriener, K. Segawa, K. Yada, Y. Tanaka, M. Sato, and Y. Ando, *Phys. Rev. Lett.* **107**, 217001 (2011).
⁹ D. Chevallier, D. Sticlet, P. Simon, and C. Bena, *Phys. Rev. B* **85**, 235307 (2012).
¹⁰ D. Sticlet, C. Bena, and P. Simon, *Phys. Rev. Lett.* **108**, 096802 (2012).
¹¹ J. Klinovaja, A. Yacoby, and D. Loss, *Phys. Rev. B* **90**, 155447 (2014).
¹² R. M. Lutchyn, J. D. Sau, and S. Das Sarma, *Phys. Rev. Lett.* **105**, 077001 (2010).
¹³ Y. Oreg, G. Refael, and F. von Oppen, *Phys. Rev. Lett.* **105**, 177002 (2010).
¹⁴ J. Alicea, *Phys. Rev. B* **81**, 125318 (2010).
¹⁵ L. Mao, M. Gong, E. Dumitrescu, S. Tewari, and C. Zhang, *Phys. Rev. Lett.* **108**, 177001 (2012).
¹⁶ M. Kjaergaard, K. Wölms, and K. Flensberg, *Phys. Rev. B* **85**, 020503 (2012).
¹⁷ J. Klinovaja, P. Stano, and D. Loss, *Phys. Rev. Lett.* **109**, 236801 (2012).
¹⁸ A. C. Potter and P. A. Lee, *Phys. Rev. B* **83**, 094525 (2011).
¹⁹ J. Klinovaja, P. Stano, A. Yazdani, and D. Loss, *Phys. Rev. Lett.* **111**, 186805 (2013).
²⁰ B. Braunecker and P. Simon, *Phys. Rev. Lett.* **111**, 147202 (2013).
²¹ M. M. Vazifeh and M. Franz, *Phys. Rev. Lett.* **111**, 206802 (2013).
²² J. Klinovaja, S. Gangadharaiah, and D. Loss, *Phys. Rev. Lett.* **108**, 196804 (2012).
²³ J. Klinovaja, G. J. Ferreira, and D. Loss, *Phys. Rev. B* **86**, 235416 (2012).
²⁴ J. Klinovaja and D. Loss, *Phys. Rev. X* **3**, 011008 (2013).
²⁵ C. Dutreix, M. Guigou, D. Chevallier, and C. Bena, *arXiv:1309.1143*.
²⁶ J. Klinovaja and D. Loss, *Phys. Rev. B* **88**, 075404 (2013).
²⁷ V. Mourik, K. Zuo, S. M. Frolov, S. R. Plissard, E. P. A. M. Bakkers, and L. P. Kouwenhoven, *Science* **336**, 1003 (2012).
²⁸ A. Das, Y. Ronen, Y. Most, Y. Oreg, M. Heiblum, and H. Shtrikman, *Nat. Phys.* **8**, 887 (2012).
²⁹ M. T. Deng, C. L. Yu, G. Y. Huang, M. Larsson, P. Caroff, and H. Q. Xu, *Nano Lett.* **12**, 6414 (2012).
³⁰ L. P. Rokhinson, X. Liu, and J. K. Furdyna, *Nat. Phys.* **8**, 795 (2012).
³¹ J. R. Williams, A. J. Bestwick, P. Gallagher, S. S. Hong, Y. Cui, A. S. Bleich, J. G. Analytis, I. R. Fisher, and D. Goldhaber-Gordon, *Phys. Rev. Lett.* **109**, 056803 (2012).
³² H. O. H. Churchill, V. Fatemi, K. Grove-Rasmussen, M. T. Deng, P. Caroff, H. Q. Xu, and C. M. Marcus, *Phys. Rev. B* **87**, 241401 (2013).
³³ D. Rainis and D. Loss, *arXiv:1407.8239*.
³⁴ C. Kloeffer, M. Trif, and D. Loss, *Phys. Rev. B* **84**, 195314 (2011).
³⁵ X.-J. Hao, T. Tu, G. Cao, C. Zhou, H.-O. Li, G.-C. Guo, W. Y. Fung, Z. Ji, G.-P. Guo, and W. Lu, *Nano Lett.* **10**, 2956 (2010).
³⁶ L. J. Lauhon, M. S. Gudiksen, D. Wang, and C. M. Lieber, *Nature* **420**, 57 (2002).
³⁷ W. Lu, J. Xiang, B. P. Timko, Y. Wu, and C. M. Lieber, *Proc. Natl. Acad. Sci. USA* **102**, 10046 (2005).
³⁸ J. Xiang, A. Vidan, M. Tinkham, R. M. Westervelt, and C. M. Lieber, *Nat. Nanotech.* **1**, 208 (2006).
³⁹ J. Xiang, W. Lu, Y. Hu, Y. Wu, H. Yan, and C. M. Lieber, *Nature* **441**, 489 (2006).
⁴⁰ Y. Hu, H. O. H. Churchill, D. J. Reilly, J. Xiang, C. M. Lieber, and C. M. Marcus, *Nat. Nanotech.* **2**, 622 (2007).
⁴¹ H. Yan, H. S. Choe, S. Nam, Y. Hu, S. Das, J. F. Klemic, J. C. Ellenbogen, and C. M. Lieber, *Nature* **470**, 240 (2011).
⁴² J. Nah, D. C. Dillen, K. M. Varahramyan, S. K. Banerjee, and E. Tutuc, *Nano Lett.* **12**, 108 (2012).
⁴³ Y. Hu, F. Kuemmeth, C. M. Lieber, and C. M. Marcus, *Nat. Nanotech.* **7**, 47 (2012).
⁴⁴ J.-S. Park, B. Ryu, C.-Y. Moon, and K. J. Chang, *Nano Lett.* **10**, 116 (2010).
⁴⁵ F. Maier, T. Meng, and D. Loss, *Phys. Rev. B* **90**, 155437 (2014).
⁴⁶ S. Roddaro, A. Fuhrer, C. Fasth, L. Samuelson, J. Xiang, and C. M. Lieber, *arXiv:0706.2883*.
⁴⁷ S. Roddaro, A. Fuhrer, P. Brusheim, C. Fasth, H. Q. Xu, L. Samuelson, J. Xiang, and C. M. Lieber, *Phys. Rev. Lett.* **101**, 186802 (2008).
⁴⁸ A. P. Higginbotham, T. W. Larsen, J. Yao, H. Yan, C. M. Lieber, C. M. Marcus, and F. Kuemmeth, *Nano Lett.* **14**, 3582 (2014).
⁴⁹ A. P. Higginbotham, F. Kuemmeth, T. W. Larsen, M. Fitzpatrick, J. Yao, H. Yan, C. M. Lieber, and C. M. Marcus, *Phys. Rev. Lett.* **112**, 216806 (2014).

- ⁵⁰ F. Maier, C. Kloeffer, and D. Loss, Phys. Rev. B **87**, 161305 (2013).
- ⁵¹ C. Kloeffer, M. Trif, P. Stano, and D. Loss, Phys. Rev. B **88**, 241405 (2013).
- ⁵² N. Ares, V. N. Golovach, G. Katsaros, M. Stoffel, F. Fournel, L. I. Glazman, O. G. Schmidt, and S. De Franceschi, Phys. Rev. Lett. **110**, 046602 (2013).
- ⁵³ N. Ares, G. Katsaros, V. N. Golovach, J. J. Zhang, A. Prager, L. I. Glazman, O. G. Schmidt, and S. De Franceschi, Applied Physics Letters **103**, 263113 (2013).
- ⁵⁴ E. Prada, P. San-Jose, and R. Aguado, Phys. Rev. B **86**, 180503 (2012).
- ⁵⁵ S. Das Sarma, J. D. Sau, and T. D. Stanescu, Phys. Rev. B **86**, 220506 (2012).
- ⁵⁶ D. Rainis, L. Trifunovic, J. Klinovaja, and D. Loss, Phys. Rev. B **87**, 024515 (2013).
- ⁵⁷ J. J. Zhang, G. Katsaros, F. Montalenti, D. Scopece, R. O. Rezaev, C. Mickel, B. Rellinghaus, L. Miglio, S. De Franceschi, A. Rastelli, and O. G. Schmidt, Phys. Rev. Lett. **109**, 085502 (2012).
- ⁵⁸ J. Klinovaja and D. Loss, arXiv:1408.3366.
- ⁵⁹ P. Lawaetz, Phys. Rev. B **4**, 3460 (1971).
- ⁶⁰ R. Winkler, *Spin-Orbit Coupling Effects in Two-Dimensional Electron and Hole Systems* (Springer-Verlag, Berlin, 2003).
- ⁶¹ S. Bravyi, D. P. DiVincenzo, and D. Loss, Ann. Phys. (NY) **326**, 2793 (2011).
- ⁶² J. Klinovaja and D. Loss, Phys. Rev. B **86**, 085408 (2012).
- ⁶³ D. Futterer, M. Governale, U. Zülicke, and J. König, Phys. Rev. B **84**, 104526 (2011).
- ⁶⁴ A. G. Moghaddam, T. Kernreiter, M. Governale, and U. Zülicke, Phys. Rev. B **89**, 184507 (2014).
- ⁶⁵ To avoid confusion between various holes, please note that the hole mentioned here actually denotes the conjugate hole.
- ⁶⁶ A. A. Zyuzin, D. Rainis, J. Klinovaja, and D. Loss, Phys. Rev. Lett. **111**, 056802 (2013).
- ⁶⁷ Y. Oreg, E. Sela, and A. Stern, Phys. Rev. B **89**, 115402 (2014).
- ⁶⁸ J. Klinovaja and D. Loss, Phys. Rev. B **90**, 045118 (2014).
- ⁶⁹ J. Klinovaja and D. Loss, Phys. Rev. Lett. **112**, 246403 (2014).
- ⁷⁰ J. C. Y. Teo and C. L. Kane, Phys. Rev. B **89**, 085101 (2014).
- ⁷¹ J. Klinovaja and D. Loss, Phys. Rev. Lett. **111**, 196401 (2013).
- ⁷² T. Neupert, C. Chamon, C. Mudry, and R. Thomale, arXiv:1403.0953.
- ⁷³ T. Meng, P. Stano, J. Klinovaja, and D. Loss, Eur. Phys. J. B **87**, 203 (2014).
- ⁷⁴ J. Klinovaja and D. Loss, Eur. Phys. J. B **87**, 171 (2014).
- ⁷⁵ I. Seroussi, E. Berg, and Y. Oreg, Phys. Rev. B **89**, 104523 (2014).
- ⁷⁶ E. Sagi and Y. Oreg, arXiv:1403.1791.
- ⁷⁷ J. Klinovaja and Y. Tserkovnyak, Phys. Rev. B **90**, 115426 (2014).